Neurobiology of Disease 160 (2021) 105528

Contents lists available at ScienceDirect

Neurobiology of Disease

journal homepage: www.elsevier.com/locate/ynbdi

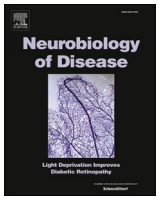

Autofluorescent imprint of chronic constriction nerve injury identified by deep learning

Martin E. Gosnell [a], Vasiliki Staikopoulos [b,c,1], Ayad G. Anwer [d,e,1], Saabah B. Mahbub [d,e], Mark R. Hutchinson [b,c], Sanam Mustafa [b,c], Ewa M. Goldys [d,e,*]

[a] Quantitative Pty Ltd, 118 Great Western Highway, Mount Victoria, NSW 2786, Australia
[b] ARC Centre of Excellence for Nanoscale Biophotonics, University of Adelaide, Adelaide 5005, Australia
[c] Adelaide Medical School, University of Adelaide, Adelaide 5005, Australia
[d] ARC Centre of Excellence for Nanoscale Biophotonics, UNSW Sydney, NSW 2052, Australia
[e] Graduate School of Biomedical Engineering, UNSW Sydney, NSW 2052, Australia

ARTICLE INFO

Keywords:
Chronic pain
Autofluorescence imaging
Spinal cord
Allodynia
Nerve injury
Deep learning
Chronic constriction injury (CCI)

ABSTRACT

Our understanding of chronic pain and the underlying molecular mechanisms remains limited due to a lack of tools to identify the complex phenomena responsible for exaggerated pain behaviours. Furthermore, currently there is no objective measure of pain with current assessment relying on patient self-scoring. Here, we applied a fully biologically unsupervised technique of hyperspectral autofluorescence imaging to identify a complex signature associated with chronic constriction nerve injury known to cause allodynia. The analysis was carried out using deep learning/artificial intelligence methods. The central element was a deep learning autoencoder we developed to condense the hyperspectral channel images into a four- colour image, such that spinal cord tissue based on nerve injury status could be differentiated from control tissue.

This study provides the first validation of hyperspectral imaging as a tool to differentiate tissues from nerve injured vs non-injured mice. The auto-fluorescent signals associated with nerve injury were not diffuse throughout the tissue but formed specific microscopic size regions. Furthermore, we identified a unique fluorescent signal that could differentiate spinal cord tissue isolated from nerve injured male and female animals. The identification of a specific global autofluorescence fingerprint associated with nerve injury and resultant neuropathic pain opens up the exciting opportunity to develop a diagnostic tool for identifying novel contributors to pain in individuals.

1. Introduction

Despite impacting one in five individuals worldwide, currently there are no objective measures of pain. Instead, clinicians rely on self-scoring by patients which presents many challenges when treating children and non-verbal patients. Self-reporting of pain may also lead to drug abuse potential due to misreporting. With opioids implicated in over 70% of drug-related deaths worldwide, this is a major concern (WHO, 2020).

Our understanding of pain and the underlying mechanisms is, at best, limited (Nightingale, 2012). Paradoxically, one of the major limitations preventing the advancement of knowledge is the utilisation of research methodologies which rely on our current, incomplete understanding of the mechanisms behind pain. With the exception of unbiased approaches like RNA-seq (Wang et al., 2009; Grace et al., 2012), many methodologies often measure defined proteins including those thought to play key roles in pain signalling (Jacobsen et al., 2016). Not only are these methods unable to detect currently unknown contributors to pain signalling, but they also cannot measure changes at a global level. This is important because pain mechanisms are likely to include numerous components contributing in a highly regulated manner (Grace et al., 2014).

Tissue autofluorescence is generally considered background noise in imaging studies and much effort is placed to reduce its impact on exogenous fluorescent labelling. However, this autofluorescence signal is derived from various cellular metabolites and co-enzymes of metabolic pathways critical for normal cellular functions as well in

* Corresponding author at: ARC Centre of Excellence for Nanoscale Biophotonics, UNSW Sydney, NSW 2052, Australia.
E-mail address: e.goldys@unsw.edu.au (E.M. Goldys).
[1] These authors contributed equally.

https://doi.org/10.1016/j.nbd.2021.105528
Received 7 May 2021; Received in revised form 1 October 2021; Accepted 4 October 2021
Available online 7 October 2021

pathophysiological signal transduction. These include nicotinamide adenine dinucleotide (NAD) and nicotinamide adenine dinucleotide phosphate (NADPH) which have been implicated in neuropathic pain via their generation of reactive oxygen species (Grace et al., 2016). Acting as a signalling molecule, ROS contributes towards metabolic dysfunction and inflammatory signalling. Therefore, this highlights the potential to exploit the autofluorescence characteristics of the metabolic pathway to ultimately identify an autofluorescence fingerprint associated with chronic pain.

Autofluorescence hyperspectral imaging, is a sophisticated label-free technology that is capable of identifying endogenous fluorescent signals from cells and tissues with the use of multiple excitation and emission wavelengths. Previous studies have reported the use of autofluorescence hyperspectral imaging to reveal subtle signatures of cell metabolic activity, which are reflected in complex physiological processes such as neurodegeneration (Gosnell et al., 2016a) or cancer (Habibalahi et al., 2019a) and the identification of developmentally healthy bovine embryos (Monteiro et al., 2021). To date, there have been no studies identifying the complex autofluorescence signature associated with peripheral nerve injury and subsequent chronic pain. By exploring the utility of natural tissue autofluorescence as a global marker of metabolic change caused by nerve injury and its associated development of neuropathic pain, this study will overcome limitations of targeted approaches which assume the involvement of specific cells or proteins.

In this study, we determine if hyperspectral imaging has the potential to differentiate spinal cord tissue derived from control and an established neuropathic pain model of chronic constriction injury (CCI) (Grace et al., 2014). The CCI mouse model uses chromic gut sutures placed subcutaneously and around the sciatic nerve which cause nerve injury and induce nociceptive hypersensitivity and neuroimmune adaptations at the level of the lumbar spinal cord dorsal horn. This model has been shown to produce mid to high degree of allodynia, which is relevant to clinical human chronic pain presentation (Grace et al., 2012). Following hyperspectral autofluorescent image acquisition, quantitative image analysis to extract mathematical features of spectral and spatial distribution of autofluorescence was conducted to uncover subtle hitherto hidden signatures of CCI. In an extension to this study, we investigated if the autofluorescent signatures in male and female CCI mice was unique and whether hyperspectral imaging was able to identify these.

2. Materials and methods

2.1. Grace model of chronic constriction nerve injury-induced neuropathic pain

2.1.1. Subjects

Pathogen-free adult male and female Balb/c mice (20–25 g; Laboratory Animal Services, University of Adelaide) were used in all experiments. Mice were housed in temperature (18–21 degree C) and light-controlled (12 h light/dark cycle; lights on at 07:00 h) rooms with standard rodent food and water available ad libitum and allowed to habituate to the holding facility for 1 week prior to experimentation. All procedures were approved by the Animal Ethics Committee of the University of Adelaide (M-2013-277) and were conducted in accordance with the NHMRC Australian Code of Practice for the Care and Use of Animals for Scientific Purposes (8th edition 2013). Sample sizes were based on our experience in our previous publication (Grace et al., 2010) that allowed for adequate power to account for behavioural variance which is classically normally distributed in this model of pain. Owing to the novel nature of the imaging approach applied here we chose this proven approach as variance in the hyperspectral imaging could not be predicted a priori. Animals were randomly assigned to groups at the time of surgery by the surgeon conducting the chronic constriction injury.

2.1.2. Groups and design

The chronic constriction injury (CCI model) adapted by Grace *et al*[11], using 1–4 chromic gut sutures around the sciatic nerve, was modified by ligating the sciatic nerve (N) with 3 chromic gut sutures and 1 suture placed subcutaneously (S) over the hip to control for the inflammatory component that contributes to the nociceptive hypersensitivity associated with the CCI model (Grace et al., 2010). This model has been shown to produce mid to high degree of allodynia, which is relevant to clinical human pain presentation. Mice with 0 sutures around the sciatic nerve had 4 chromic gut pieces placed subcutaneously over the hip, such that each treated animal was exposed to a total of 4 chromic gut pieces of equivalent length, and hence the same systemic inflammatory challenge. The treatment groups used were separate groups of male and female mice N0S4 (sham surgery), N3S1 (nerve injury group, CCI surgery) and N0S0 (no surgery control). Animals were followed to postoperative (PO) day 21 to allow for the development of neuropathy and underwent behavioural von Frey testing confirming mechanical allodynia.

In our analysis, we combined our control and sham animals into one control group (70% of all animals) as this encourages the search to be based in a discriminant space characterised by minimal individual animal differences (intra class). Such a grouping also encourages a discriminant space which is minimally affected by the surgery and anaesthesia. Data shown in Fig. 2, Figs. 3-6 and Fig. 7 were from 3 different animal cohorts (n - number of animals: Fig. 2: male: N3S1 - $n = 5$, N0S4 - $n = 5$, N0S0 - $n = 4$, Figs. 3-6: male: N3S1 - $n = 4$, N0S4 - $n = 4$, N0S0 - $n = 5$; female: N3S1 - $n = 8$, N0S4 - $n = 7$, N0S0 - $n = 8$; Fig. 7: male: N3S1 - $n = 1$, N0S4 - $n = 1$, N0S0 - $n = 1$ examples for image presentation).

2.1.3. Surgery

The Grace CCI model of sciatic nerve injury (Grace et al., 2010) was performed at the mid-thigh level of the left hindleg. Briefly, animals were anesthetised with isofluorane (2% in oxygen), the shaved skin was cleansed with 100% ethanol and the surgery was aseptically performed. Zero or 3 sterile chromic gut sutures (cuticular 4–0 chromic gut, FS-2; Ethicon, Somerville, NJ, USA) were loosely tied around the gently isolated sciatic nerve. Once the superficial muscle overlying the nerve was sutured, additional lengths of chromic gut (4 or 1) were placed subcutaneously. No surgical intervention was conducted on the control group (N0S0). Animals were monitored postoperatively until fully ambulatory prior to return to their home cage and checked daily for any sign of infection.

2.1.4. von Frey testing of mechanical allodynia

The Nicotra method of von Frey testing (Nicotra et al., 2014) was performed by an independent tester who was blinded to group assignment. Briefly, mice underwent a week of habituation to the von Frey apparatus prior to testing. Baseline testing was taken at day 0 prior to surgery with subsequent behavioural assessment taken at days 1, 5, 7, 14 and 21 following surgery allowing for a verification of the anticipated allodynia as per ethics approval requirements. For testing, mice were subjected to 10 stimulations with 6 calibrated von Frey filaments (2.44, 2.83, 3.22, 3.61, 3.84 and 4.08 g). von Frey filaments were applied for 1 s at 1 s intervals. Filaments were not applied in ascending order of force, but rather random assignment each test session. To avoid sensitisation, 10 min break was given between each set of stimulations, with 10 stimulations per filament. The response frequency at each von Frey filament and behavioural responses were recorded as the average number of responses out of 10 for each von Frey stimulus. The percentage withdrawal responses to von Frey filaments was calculated based on the total number of responses to all filaments applied at each hind paw (ipsilateral and contralateral) demonstrating that allodynia was stable on PO Day 21.

2.2. Preparing tissue for imaging

Following von Frey testing on day 21 post-surgery, mice were humanely killed with an i.p. overdose of sodium pentobarbital (60 mg/kg). Animals then underwent transcardial perfusion with 0.9% saline to clear the blood from the organs before the spinal lumbar enlargement was quickly dissected and snap frozen in liquid nitrogen. The tissue was then embedded in OCT (Tissue Tek Compound, Sakura Finetek, USA) before cutting at 10um on the cryostat, mounted onto glass coverslips and stored at minus 80 degrees prior to imaging. Tissue was taken to include the lumbar segment 3, 4 and 5 (L3, L4 and L5) of the spinal cord which is innervated by both the injured (ipsilateral) and non-injured (contralateral) sciatic nerves. These regions have been reported to exhibit changes following nerve injury (Mahbub, 2017).

2.3. Hyperspectral imaging system

An adapted fluorescence microscope (Olympus iX71™) was used in this work with a 40× water U12™ series objective (with wide transmission in UV range). LEDs with excitation wavelength bands centred at 334, 375, 365, 385, 395, 405, 415, 425, 435, 455, 475, 495 nm, each about 10 nm wide produced close to monochromatic light to excite tissue auto-fluorescence. The corresponding tissue emission was measured with three epifluorescence filter cubes with the emission bands centred at 447 nm (60 nm wide), 587 nm (35 nm wide) and 700 nm long pass. Overall, in this work we used spectral channels as listed in Supplementary Table 1), and each field of view was imaged in all these channels forming a hyperspectral image. All images were captured by an iXON™ 885 DU EMCCD camera (Andor Technology Ltd., UK) with image size 1002 × 1004 pixels.

2.4. Hyperspectral imaging data preparation and image analysis

To exclude any autofluorescence bias caused by white versus grey matter within the spinal cord, regions of interest (ROIs) of relevant images were selected to limit the analysis to the grey matter of the dorsal horn. This region processes sensory information, which is then transmitted to several higher brain regions, including those responsible for pain perception. All hyperspectral images underwent conditioning which consist of filtering using a log-gabor phase preserving wavelet filter, background removal, calibration, and non-uniformity reduction by fitting a common, channel-dependent illumination function to each channel of the data set (Campbell et al., 2020a; Campbell et al., 2019; Campbell et al., 2020b; Habibalahi et al., 2019b; Habibalahi et al., 2020; Mahbub, 2017; Mahbub et al., 2017; Singh et al., 2014).

Only the ipsilateral (ipsi) images are analysed, the corresponding contralateral (contra) images are used as controls, whereby each ipsilateral spectral image had subtracted from it, the mean spectra of the corresponding contralateral tissue image. The data is then standardised by setting the mean of each variable to zero and the standard deviation to one. For the nerve injury projection carried out by the autoencoder (Møller, 1993), the variables values are linearly transformed to fit into a range between −0.5 and 0.5.

2.5. Immunofluorescence

In a separate group of male animals which had undergone similar surgery as outlined above (control, sham operated and CCI operated), spinal cord tissue perfused with 0.9% saline followed by 4% paraformaldehyde (4% PFA) was collected and prepared for cryostat cutting. Briefly, tissue was placed in 4% PFA overnight followed by 3 × 10 min washes in PBS (0.01 M) then placed in 20% sucrose - PBS overnight. Lumbar segment 4 (L4) was separated and frozen in OCT (Optimal Cutting Temperature solution) and cut on the cryostat (10 um) and placed onto Superfrost plus™ glass slides. The tissue sections were allowed to air dry for an hour at room temperature before being processed for immunofluorescence (IF). The sections were blocked for 1 h at room temperature with 1% BSA in PBS - Triton (0.3%), followed by a two-night incubation at 4 degrees with the following primary antibody combinations made up in blocking buffer; 1) Rabbit anti CGRP (Sigma-Aldrich Australia C8198; 1:500) and Goat anti IBA1 (Sigma-Aldrich Australia SAB2500041; 1:500), 2) Rabbit anti CGRP (Sigma-Aldrich Australia C8198; 1:500) and Mouse anti GFAP (G85) conjugated to Alexa Fluor 488 (eBiosciences 53–9892-82; 1:2000). Sections were then washed 3 × 10 min with PBS - Triton (0.3%) followed by an hour incubation in secondary antibody; Donkey at Rabbit (IgG) 594 Alexa Fluor (Molecular Probes A21207; 1:1000), Donkey anti Goat (IgG) 488 Alexa Fluor (Molecular Probes A11055; 1:1000) and DAPI nuclear stain (Invitrogen D1306; 1:10,000) at room temperature. Following 3 × 10 min washes in PBS, sections were then placed on coverslips using antifade aqueous mounting media (PST: IM030). Images of the immunofluorescence staining were taken at the following wavelengths (405 laser: 461/359 nm emission/excitation; 594 laser: 618/590 nm emission/excitation; 488 laser: 520/488 nm emission/excitation) on an Olympus confocal scanning microscope (FV3000) using a 60× silica (NA 1.4) objective.

2.6. Quantification of immunofluorescence images

To assess changes in immunofluorescent staining for each of the markers using Image J (Fiji; version 2.1.0/1.53c). Briefly, the Integrated Density of CGRP was measured in the outer laminae (L1−2) of the ipsilateral dorsal horn from 3 sections of each treatment group and the mean determined and compared using one-way ANOVA. Changes in glial staining patterns, (such as cell numbers and morphology) were observed in both superficial and deeper laminae layers of the dorsal horn, therefore we measured the number of cells in three randomly assigned 100 × 100 um boxes along the laminae 1–4 region from 3 sections of each treatment group and determined the mean and compared using one-way ANOVA. Data was expressed as mean ± SEM and significance determined when $p < 0.05$.

2.7. Statistics

Kolmogorov-Smirnov, ordinary one-way ANOVA and two-way ANOVA tests were used to establish statistical significance (Massey Jr, 1951). Significance levels are marked with *, **,*** and # and *p*-values are given in the respective figures. Generally, differences were considered significant for $p < 0.05$.

2.8. Code availability

Software developed for this project is available upon request from Quantitative Pty Ltd.

3. Results

3.1. Overview of bioinformatics analysis in this work

We first identified broad autofluorescent differences in the spinal cord tissue which correlated with CCI. We then tested the hypothesis that this autofluorescent signature will cluster spatially and will overlay specific cells in the dorsal spinal cord. We also investigated the existence of a sex-dependent autofluorescence signature. To visualise the CCI-affected regions we developed a sophisticated hyperspectral "CCI colour" projection method, condensing multichannel hyperspectral images into four variables (CMYK). We performed an in-depth discriminatory analysis on the tissue segments comprising CCI-activated pixels allowing us to compare CCI and control groups. This has confirmed that microscopic-sized areas within spinal cord tissue sections are different in the CCI and control groups. We quantified the spatial distribution of the autofluorescent signature in male and female models of CCI. We verified

that the observed differences are not an artefact of the analysis. Our final cross-discriminatory analysis is consistent with the finding that male and female autofluorescent colour associated with CCI is different. The schematic diagram of our analysis is shown in Fig. 1.

3.2. Spinal autofluorescence signatures linked to nerve-injury

Hyperspectral autofluorescence signature related to CCI and behavioural allodynia was explored in the post-mortem lumbar spinal cord tissue images from the dorsal horn from male mice and compared to sham injured and control mice. The presence of mechanical allodynia was confirmed at day 21 following CCI surgery in the left (ipsilateral) hind-paw of both male and female mice. No allodynia was observed in the right (contralateral) hind-paw of CCI injured animals or either hind-paw of sham or control animals. (Supplementary Fig. 1).

In order to verify that an autofluorescent signature can identify tissue from the CCI animal group from similar (L4) (Rigaud et al., 2008) tissue isolated from the control and sham groups, several regions were extracted from the centre of each tissue image. Each of these regions represents a random selection of 10 rectangles each approximately 15 μm × 15 μm in size (Supplementary Fig. 2). For each of these regions, a vector of spectral and spectral morphology features was calculated as described in Supplementary Material Note 1; these features are sensitive to the biochemistry in that region (Habibalahi et al., 2019a; Mahbub et al., 2017; Gosnell et al., 2016b; Mahbub et al., 2019; Mahbub et al., 2021). A linear discriminant analysis (LDA) was carried out (Gosnell et al., 2016a; Gosnell et al., 2016b) using the vectors of features extracted from autofluorescent signatures of L4 tissue, to maximally discriminate the nerve-injured and control groups which produced clusters shown in Fig. 2. By projecting these data onto a single discriminating variable, we found that the hyperspectral signature from nerve-injured tissue could clearly differentiate tissue from control and sham animals (Supplementary Fig. 2 a, h). This means that the autofluorescent signatures allow accurate classification of the nerve-injured and control groups.

3.3. Deep learning algorithm identifies the "CCI projection"

We developed a deep learning algorithm to create an expertly interpreted version of hyperspectral image datasets which highlight CCI-related tissue signatures. The algorithm compresses the highly dimensional hyperspectral data into exactly four colour (CMYK) variables (Møller, 1993) (see Supplementary Methods Note 2, Supplementary Fig. 3), enabling clear visualisation of regions where the autofluorescence was modified by nerve injury. A network topology where the output data at each iterative step have the same dimension (image size) as the input data enabled the algorithm to be iteratively trained. Example tissue images processed by this algorithm are illustrated in Supplementary Fig. 4. The 'CCI projection' images optimally visualise CCI-induced changes in tissue autofluorescent signatures relative to known anatomical regions within the spinal cord responsible for pain processing.

3.4. Search algorithm creates "CCI masks" for isolating biological targets

We further sought to identify if the nerve injury signal detected in the images is localised to specific biologically relevant tissue areas. To this end, we developed a search algorithm in order to identify selected pixels in our hyperspectral images which correlate with allodynia and create masks. The algorithm was designed to search for cell-size segments in the nerve injury-affected tissue that are significantly spectrally different (in the pixel feature space) to similar segments in the control-sham tissue. A set of candidate masks was produced by feature selection from Cohort 3 L3 tissue, as described in Supplementary Methods Note 3. We then identified the best masks from our candidate set which met the criteria: (1) the masked segments being similar in size and shape to cells using an expert guided comparative histology approach (Treuting et al., 2017); (2) being created using a channel ratio feature image known to have a metabolic meaning (Gosnell et al., 2016b); and (3) providing significant group discrimination between the control-sham and nerve-injured animals across the entire animal set. The top 97 (out of ~1800) highest distance-scoring feature masks were examined for compliance with the above criteria. The best mask (Mask 630) is shown in Supplementary Figs. 5–23. Therefore the 'CCI mask', (Mask 630), allows for optimal identification of structural features throughout the tissue image based on specific hyperspectral CCI signatures. For ease of visualisation, the hyperspectral tissue images have been processed by using our "CCI projection" (Section 3.2). The results show that this mask filters through small round-shaped areas, mostly in the order of 10–25 μm in size. The masked regions can be clearly visually discriminated

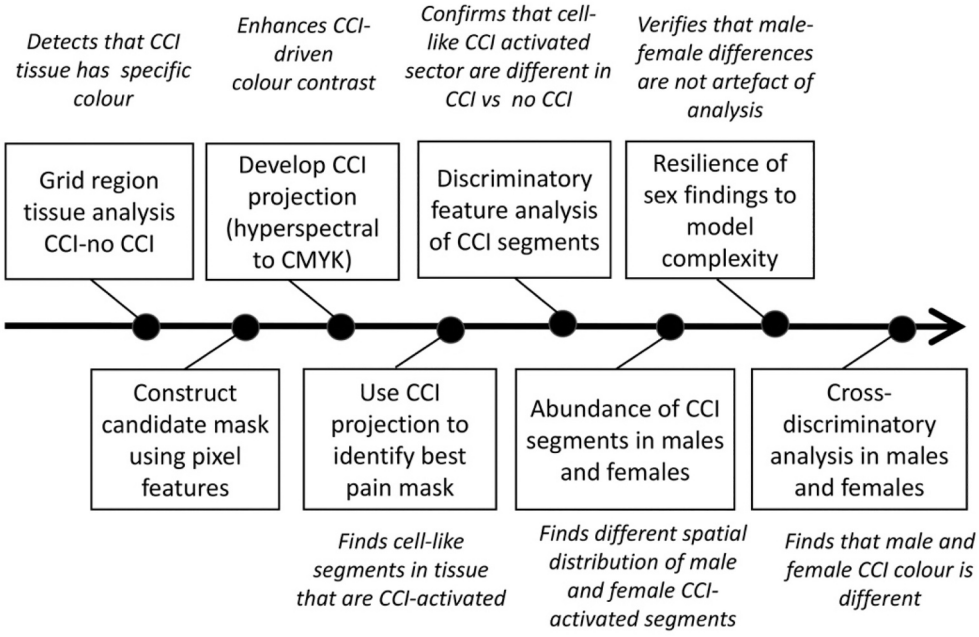

Fig. 1. Schematic diagram of the hyperspectral image analysis.

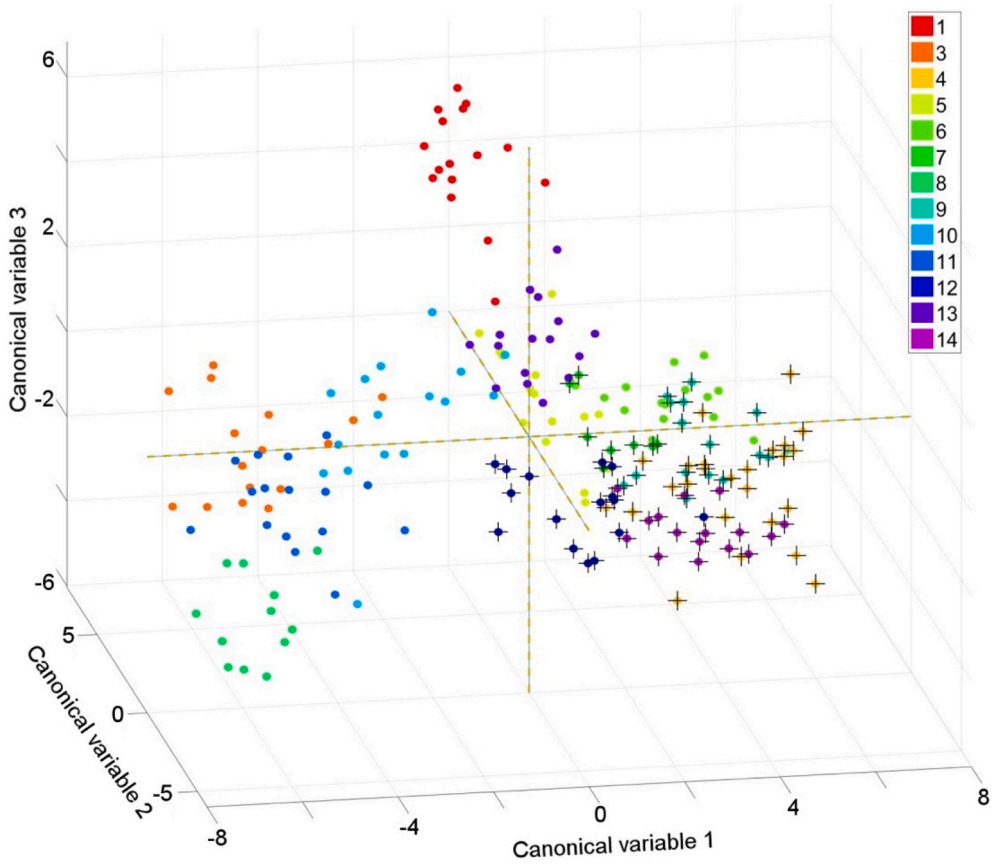

Fig. 2. Broad differences in tissue autofluorescence between CCI and control animals. Data taken from L4 tissue of male CCI group (N3S1, numbered 4,7,9,12,14, $n = 5$), and male control (N0S4, numbered 5,8,10,13 $n = 4$) and male sham (N0S4, numbered 1,2,3,6,11, n = 5). Linear discrimination analysis (LDA) projection of the eight-dimensional hyperspectral feature vectors corresponding to tissue regions from all 14 animals. Each symbol represents a single region from a tested animal. Animals are colour coded as shown on the scale. Crosses indicate regions from animals from the CCI groups. The canonical variables forming the axes are specific linear combination of the eight features utilised by this LDA.

from the surrounding tissue in the nerve-injured animals (see Supplementary Figs. 5–23). The specific feature upon which this feature mask was derived was a channel ratio intensity image of channels 6 and 8.

3.5. Discriminant analysis of "CCI masks" in the investigated groups

The feature CCI mask developed as described above isolates segments of strongly CCI-correlated pixels in the tissue images. From these segments we then generated a suite of segment features, including statistical metrics, mean, median, variance, skewness, kurtosis and entropy of both the intensity values and pairwise average intensity ratios from all available channels (see Reference (Gosnell et al., 2016b) for mathematical feature definitions). These features were assigned a group label of either "control-sham" or "CCI" and used for a discriminatory analysis. Features were generated for all 546 segments (selection shown in Supplementary Figs. 14–16. We then used sequential feature selection to identify a total of 18 features, upon which a linear discriminant model was built. The outcome for the mask 630 is illustrated in Fig. 3. This Figure confirms that tissue features calculated in the masked segments were highly distinctive between control and CCI. This finding indicates that 'CCI mask' 630 can be used to distinguish between tissue from injured and non-injured animals using specified feature sets.

3.6. Co-localisation of nuclear area with the "CCI mask"

We explored co-localisation of masked regions with individual cells in the examined tissue. A fluorescent stain, DAPI (4′,6-diamidino-2-phenylindole) was used to highlight cell nuclei in a randomly selected sample of our tissue (Fig. 4). Prior to staining, this tissue section was imaged in hyperspectral mode and transformed using our "CCI projection" to enable visualisation. The feature mask algorithm was then used to construct the matching mask (mask 630). The hyperspectral images

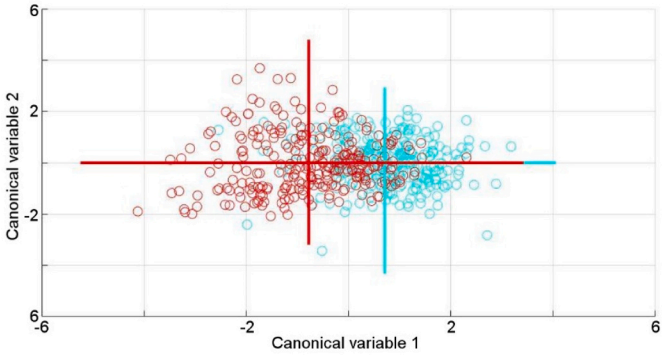

Fig. 3. Discriminatory analysis of the segments defined by the selected "CCI" mask. Results shown are for Mask 630 and they are based upon 18 intensity and intensity ratio statistical features. "CCI" segments in red, sham-control segments in blue. Statistical distance between "CCI" and sham-control clusters is 1.0872 ($p < 5.85e\text{-}46$). Data taken from L3 Cohort 3 female tissue. (For interpretation of the references to colour in this figure legend, the reader is referred to the web version of this article.)

prepared with our CCI projection algorithm were then overlaid with the mask confirming that the regions selected by the feature mask co-registered to a high degree with cell nuclei regions. The result (Fig. 4d) confirms that much of the interesting pathology captured by the feature mask throughput regions occur around cellular nuclei.

3.7. Abundance of "CCI mask" tissue

We applied the "CCI mask" (mask 630) that best fits the mask criteria to the remaining cohorts and tissue types investigated here

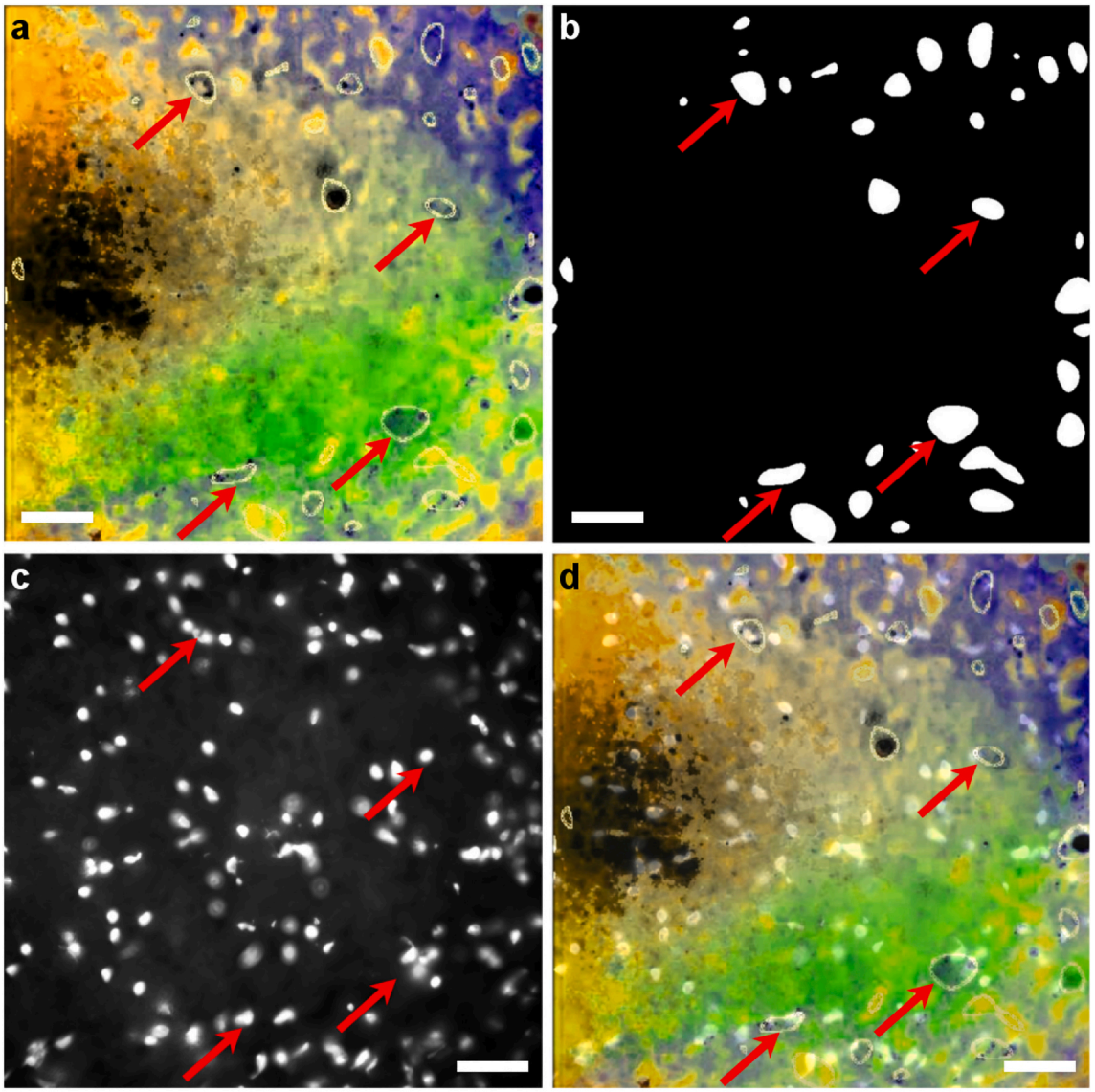

Fig. 4. Our "CCI" projection allows to highlight the CCI affected tissue areas. a) Hyperspectral tissue image after CCI projection with outlines (white) of sub-compartments extracted from the CCI mask. Red arrows point to masked CCI regions; b) The CCI mask (mask 630). c) The same section of tissue stained using DAPI highlighting cell nuclei. d) An overlay of a and c. Scale bar is 25 um. (For interpretation of the references to colour in this figure legend, the reader is referred to the web version of this article.)

(Supplementary Figs. 5–23). This generated an overview of the CCI-responsive areas in the dorsal spinal cord sections (highlighted in red in Supplementary Figs. 5–23). We then calculated the abundance factor we defined in this work as the number of individual segments selected by the mask in an image divided by the number of unmasked pixels (area of artefact-free grey matter tissue which is able to contain the CCI signal). Figs. 5a and b, respectively, show the abundance factor in males and females. The result suggests significant differences in the auto-fluorescent nerve injury-activation profile, both in males and females as we move caudally along the spinal column. We also note that the baseline in females (control-sham) appears different to the baseline in males in L4 and L5 tissue.

3.8. Robustness of discrimination of the "CCI mask" using models ranging in complexity

The CCI-activated tissue regions defined by our "CCI mask" (mask 630) allowed us to generate a suite of segment features (Section 3.4) and use them to build discriminatory models. We have further explored whether our findings depend on the complexity of our model (the number of model features used). To ensure the interpretation derived from the model was not confounded by the number of features employed we created three classes of models (F4, F9 and F18) using 4, 9 and 18 features. A total of eighteen models (one for each of the 3 tissue types L3, L4, L5 x 2 sexes x three classes of models) were built by sequentially selecting from the 1470 segment features to optimise group discrimination (control-sham and CCI). Fig. 5c shows the discriminatory performance for each tissue type, each sex and for each model class F4, F9 and F18. All models showed a consistent and highly significant difference between the male and female cohort in the L3 tissue, with the male tissue showing more pronounced discrimination between the groups than the females. The same pattern of difference was seen in the L4 tissue but to a much lesser extent, with very little difference in the L5 tissue. These findings indicate that the number of features used (ie. the complexity of the model) to discriminate between groups did not alter the findings determined by CCI mask (630).

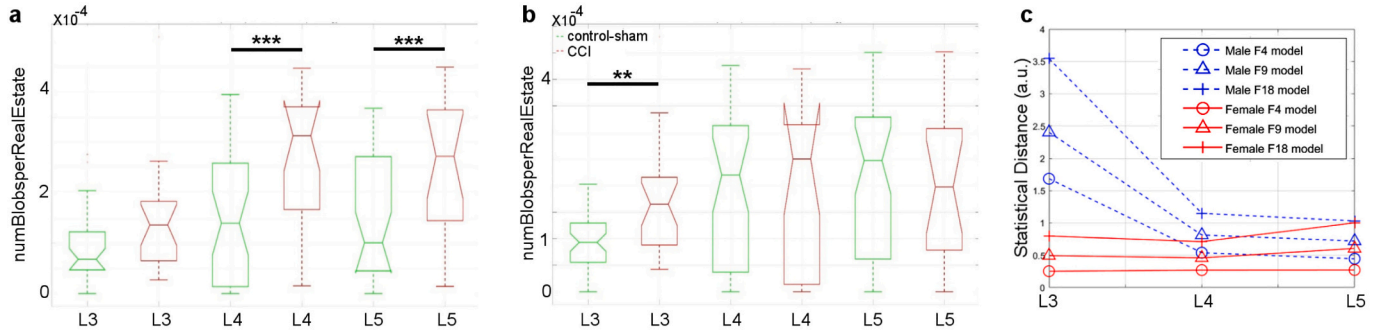

Fig. 5. (a,b) Abundance of the "CCI mask" regions. a) in male animals across L3, L4 and L5 tissue, we see significant difference between the control-sham and CCI groups with greatest differences in the L4 and L5 tissue, and no significant differences between the control-sham baseline in L3, L4 and L5 tissues ($p < 0.05$). b) in female animals across L3, L4 and L5 tissue, we see significant difference between the control-sham and CCI groups in the L3 tissue only, with significant differences in control-sham baseline seen in the L4 and L5 tissue ($p < 0.05$). c) model validation of the observed male-female differences. The statistical distance of various discriminatory models (4, 9 and 18 features, in L3, L4 and L5) is presented highlighting that the metabolic features are able to discriminate the control-sham and CCI groups to a far greater extent in males than females in the L3 tissue, similarly in other tissue to a lesser extent. p values associated with the group tests are provided in Supplementary Table 2.

3.9. Cross discriminatory analysis of males and females using the 18 feature (F18) model

To investigate whether male and female animal groups show different biochemical response to CCI, the following discriminatory test was carried out for each of the three tissue types (L3, L4, L5). We started from the F18 model in female L3 tissue which was built as previously described. We then projected onto this space the male data for same tissue type, to see how well the female model discriminates the male data. We then used the same metabolic features selected while building the female model to create a new model for the male data where the canonical weightings (eigenvectors) are recalculated to optimally discriminate the male groups, but still using only the chosen features. This addresses the questions of whether these same metabolic features contain CCI information for both sexes, and if the main discriminating vector is in a different direction for males. We repeated this process for the other two tissue types (L4 and L5).

The results for L3 tissue (Fig. 6) show that some metabolic features appear to behave differently in the male and female cohort. As this may have important mechanistic implications, we explored this in more depth by examining the highest-ranking feature chosen during the building of the female model. This feature was found to be the median of the pixel intensity ratios of channel 3 to channel 4. The analysis in Fig. 5g clearly shows that even at the univariate level this feature direction in response to CCI is significantly different across the male and female animals. The results for L4 are shown in Supplementary Figs. 24, 25 while the results for L5 are shown in Supplementary Figs. 26, 27, where the findings are closely similar to the results for L3 (Fig. 6).

3.10. Comparative immunofluorescence

To confirm that cellular and molecular changes were occurring in the spinal cord of CCI-injured animals, immunofluorescence was carried out in a subset of animals. Immunofluorescent staining of male L4 dorsal spinal cord tissue showed increased immunoreactivity of nerve terminals (CGRP), and average cell numbers of both microglia (IBA1) and astrocyte (GFAP), in the ipsilateral dorsal horn of CCI-injured animals when compared with control and sham-operated animals (Fig. 7, see quantification in Supplementary Fig. 28). Representative images show the increased CGRP staining in the outer superficial laminae of the ipsilateral dorsal horn and the increased cell density in the inner laminae (L1 - L4) of the ipsilateral dorsal horn of injured animals compared to control and sham operated. The cropped images in panel B shows the changing fluorescent staining pattern for each marker between treatment groups. These data broadly align with our findings of differences in the autofluorescence signatures between these groups.

4. Discussion

This foundational study provides the first validation of hyperspectral autofluorescence imaging as a tool to differentiate spinal cord tissues from an established model of neuropathic pain and control mice based on their autofluorescent profile. We have identified consistent global autofluorescence changes occur in spinal cord tissue of animals following chronic constriction injury and subsequent development of an exaggerated pain state called allodynia (Ji et al., 2016). The autofluorescent signals associated with nerve injury were not diffuse throughout the tissue but formed specific microscopic size regions. Excitingly, here we also report that spinal cord tissue could be further discriminated based on whether they were isolated from male or female mice. This is a critical breakthrough, as our approach overcomes the difficulty of identifying which subpopulation of the highly heterogenous dorsal horn cell population is participating in exaggerated pain. The identification of a specific global autofluorescence fingerprint associated with nerve injury and resultant neuropathic pain opens up the opportunity to develop a diagnostic tool for identifying novel contributors to pain in individuals.

The transition from acute to a chronic pain state involves critical molecular and cellular adaptations throughout peripheral and central sites within the somatosensory system, including the spinal cord (Peirs et al., 2020). The dorsal spinal cord is an important location for neuronal cell bodies and glial cells which play critical roles in chronic pain (Peirs et al., 2020). Additionally, peripheral immune cell types contribute to the central pain sensitisation processes (Grace et al., 2014). This multicellular system, communicating via diverse paracrine and autocrine molecular signalling, underpins the presentation of exaggerated pain behaviours such as hyperalgesia and allodynia (Peirs et al., 2020). The identification of currently unknown mediators of cellular events and their differentiation from bystanders is an important challenge (Peirs et al., 2020) for the understanding of the mechanisms of pain and hence the development of diagnostic tools for identifying novel contributors to pain in individuals. Therefore, adopting a non-reductionist approach is critical.

Hyperspectral imaging allows the investigation of global fluorescent changes in regions of the central nervous system (including cellular bodies and extracellular matrix) without preconceptions as to the involvement of defined cellular types. Here we have exploited naturally fluorescent metabolites and co-enzymes of metabolic pathways modified by CCI and resultant neuropathic pain to identify an associated fluorescent fingerprint in spinal cord tissue.

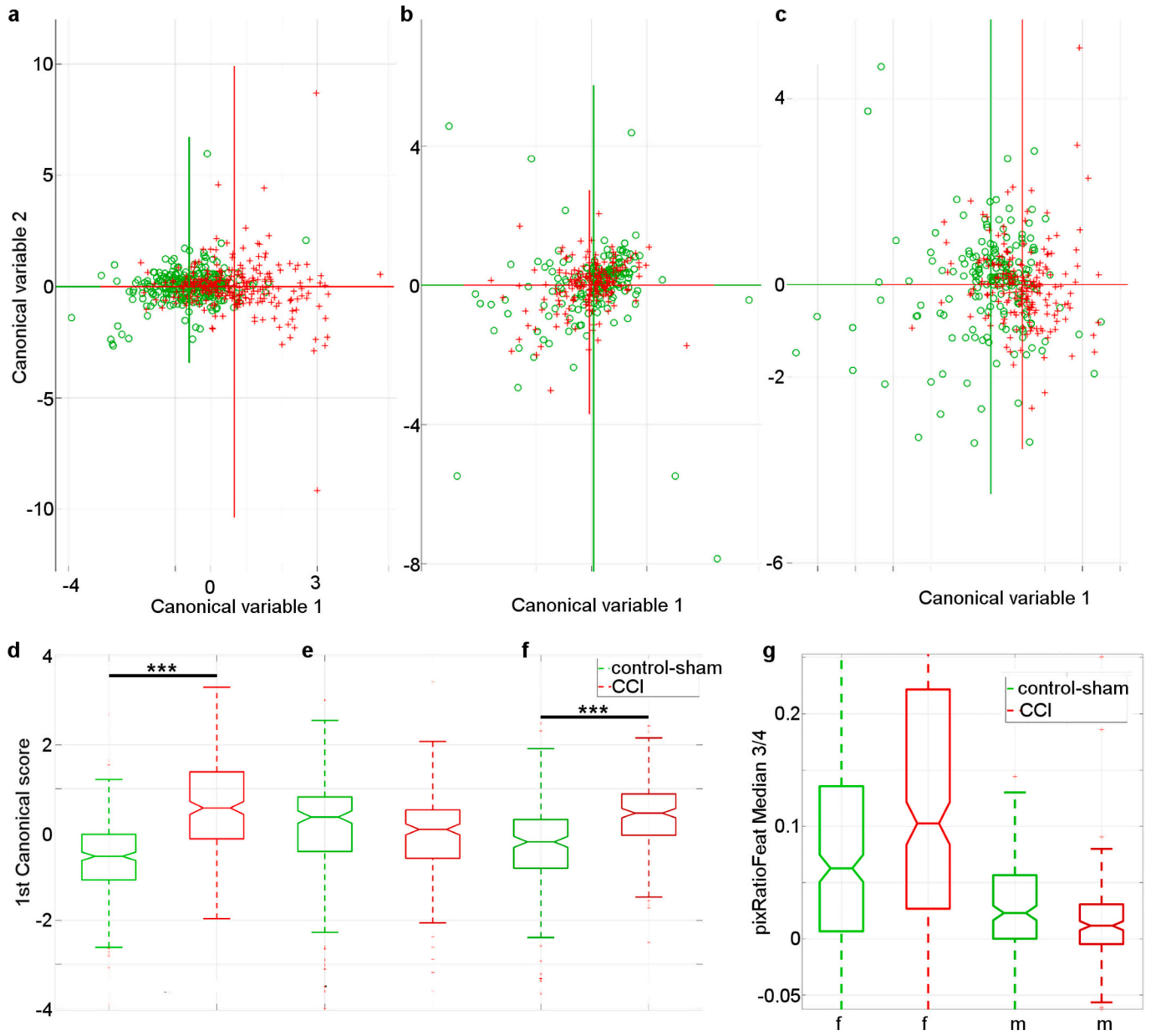

Fig. 6. Application of the same 18-feature model to males and females to further validate sex differences in the tissue. a) Discriminatory model scatter plot of Cohort 3 (female), L3 CCI-activated tissue regions, (statistical distance 0.797, $p = 2.24e\text{-}37$). b) the exact same model (the same features same discriminating vector) onto which Cohort 2 (male) data is projected shows insignificant difference (statistical distance 0.017, $p = 0.81$). (c) the same features used in female model (a) but with recalculation of the discriminating vector to suit male data shows significant discrimination (statistical distance 0.348, $p = 1.07e\text{-}15$), indicating these metabolic features are informative across sexes but that the males require a redirected discriminating vector (signature). Green – sham-control, red: CCI. (d) 1st canonical variable of Fig. 6 a, (e) 1st canonical variable of Fig. 6 b, (f) 1st canonical variable of Fig. 6 c, all shown as box plots with confidence intervals highlighted by notches. *P* values for tests of (d), (e) and (f) are p = 2.24e-37, p = 0.81, p = 1.07e-15, respectively. (g) Univariate analysis of the highest ranked feature 1, shows that there is a significant difference in the direction (control-sham(green), CCI (red)) of this segment feature across sexes (f-female, m-male). Feature 1 is the median of the pixel intensity ratios of channel 3 / channel 4. *p* values associated with the group tests are provided in Supplementary Table 3. (For interpretation of the references to colour in this figure legend, the reader is referred to the web version of this article.)

Having confirmed the existence of an autofluorescence signature of chronic constriction nerve injury (Fig. 2) we tested the hypothesis that autofluorescence from defined cell-like regions within the spinal cord tissue is altered by CCI. Using a specific feature mask which selects CCI-affected areas (Fig. 3) we have identified regions within dorsal spinal cord tissue that showed changes in autofluorescence signatures following peripheral nerve injury causing mechanical allodynia. The method developed here does not allow us to determine that our best feature mask captures all the CCI-related signal and there might be CCI-altered tissue beyond the selected mask. However, this mask best captures the CCI signal among all masks considered here, while rejecting most of the irrelevant variance.

We verified that the CCI-altered metabolic signal is present near the cellular nuclei (Fig. 4). Co-localisation of hyperspectral and DAPI images confirms that much of the interesting pathology captured by the feature mask throughout regions occur around or close to nuclei. The spinal cord is made up of neuronal and glial cells of varying sizes and shapes, both of which are important in neuropathic pain (Ji et al., 2016). Identification of individual cellular entities is beyond the scope of this work, and the hyperspectral signal reported here is likely to originate

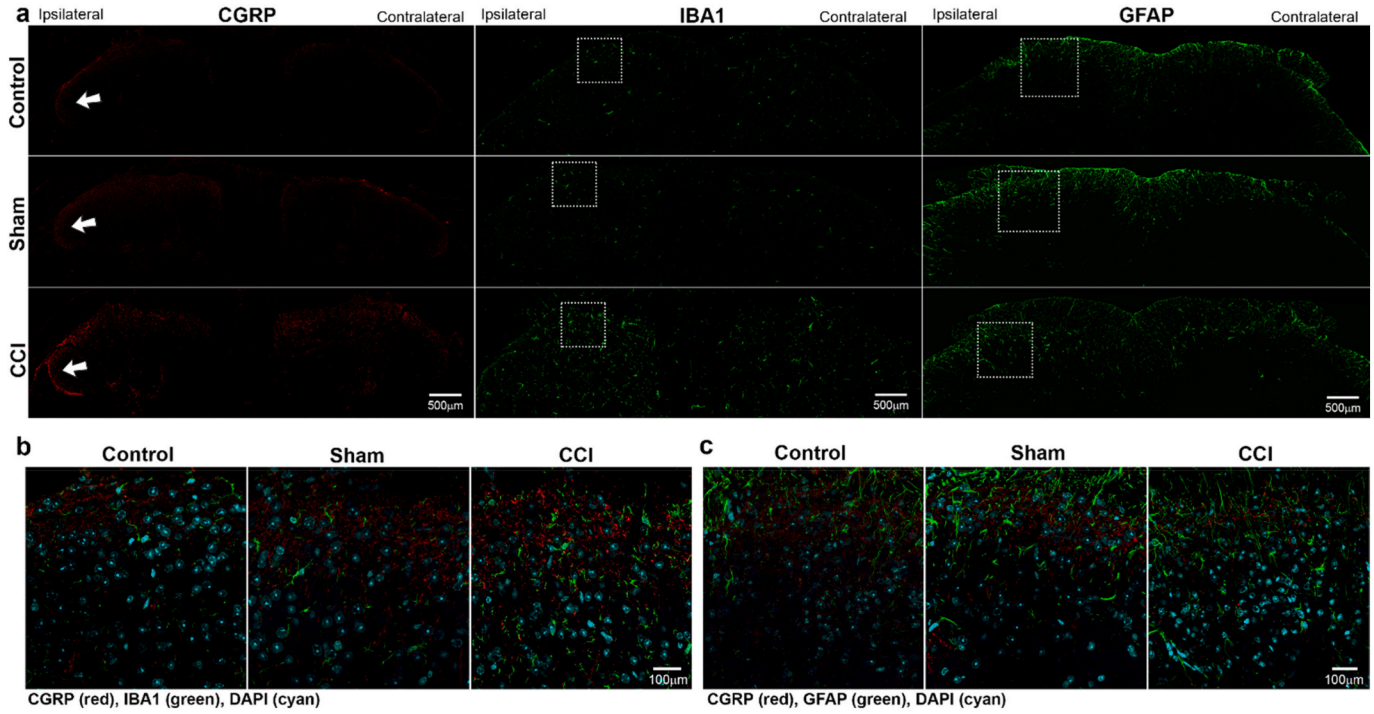

Fig. 7. Biological characterisation of immune reactivity in tissue. (a) Representative images of L4 dorsal horn from control, sham-operated and CCI animals showing immunofluorescence for CGRP (left column), IBA1 (middle column) and GFAP (right column). White dotted boxes represent the magnified images shown in (b, c). (b) Composite images for IBA1 (green), CGRP (red) and DAPI nuclear stain (cyan) and (c) GFAP (green), CGRP (red) and DAPI nuclear stain (cyan). (For interpretation of the references to colour in this figure legend, the reader is referred to the web version of this article.)

from a mix of these cells. It is worth noting that while the "CCI-affected" regions do not fully correlate with nucleated areas, the overlap of these regions with the extracellular matrix (ECM) is consistent with recent works (Tajerian and Clark, 2019) highlighting its importance in nerve injury and accompanying inflammation. The literature supports the mechanism of continuous ECM remodelling in response to its surroundings (Cox and Erler, 2011). For example, studies have shown that following injury an increase in matrix metalloproteinases is observed and, ultimately, can lead to microglial activation (Kawasaki et al., 2008). The identification of a hyperspectral signal in the ECM may be able to assist in the identification of previously unknown molecular processes following nerve injury. These would include the commonly overlooked adaptations in the glycome of the central nervous system (Jacobsen et al., 2016).

The analysis of the abundance of CCI-activated tissue regions (Fig. 5a, b) showed that there is significantly more CCI-activated tissue area in the L3 tissue nerve injury group for both females and males. This concentration around L3 likely reflects the anatomical make-up of the region and the prominence of the sciatic nerve. The male group showed significant increases in the nerve injury group in the L4 and L5 tissue, with no significant difference between the control-sham group across all tissues. The females however while showing similar increases in the L4 and L5 nerve injury, also showed increases in the control-sham group. These data are consistent with different autofluorescent CCI signatures in males and females, but they may also be influenced by different levels of allodynia observed in the male and female groups (Supplementary Fig. 1) and/or other factors, e.g. varying levels of immune reactivity due to biological variance. It is important to note that the literature supports differences between male and female chronic pain in studies carried out by traditional methods (Nicotra et al., 2014; Nicotra et al., 2012).

To eliminate the possibility of analysis artefacts we built 18 discriminatory models with a range of complexity across sexes and tissue types, all built using metabolic ratio features evaluated from the CCI-activated regions (Fig. 5c). All models showed a consistent difference between the sexes in the L3 tissue, with the male tissue showing the ability to discriminate the groups using these metabolic features to a far greater extent than the females. The same pattern of difference was seen in the L4 tissue but to a much lesser extent, with very little difference in L5. Again, this likely reflects the anatomical make-up of the region and the prominence of the injured sciatic nerve.

Cross discriminatory analysis confirmed in all cases than the metabolic features selected in optimising the female F18 models were also informative for the males, but that the direction of the discriminant shows significant difference between the groups. We further explored the eigenvector signatures (Fig. 6**)** and noted that in some cases males responded in a reverse metabolic direction for some specific features, and we demonstrated this was significant at the univariate level. These results were obtained through the application of the CCI mask (mask 630) derived from the image of the ratio of Channel 6: excitation 375 nm / emission 447 nm and Channel 8: excitation 365 nm/ emission 587 nm. The signals in these channels correspond closely to the fluorescent excitation peaks of the pyridine nucleotides NADH, NADPH and the first excitation peak of the flavin co-enzymes. Their ratio is an established marker for the cellular redox state (Campbell et al., 2020b; Mahbub et al., 2017; Mahbub et al., 2019). This suggests that the flavin:NADH ratio appears to be as a key delineator of nerve injury in males and females. This ratio is indicative of oxidative stress, which has a documented role in pain (Grace et al., 2016).

Interestingly, although the same features were critical in delineating male versus female nerve injury, the direction of the discriminant was different in males than in females, this provides an insight into the subtle complexity in cellular signalling. Although beyond the scope of this particular study, we suggest that further exploration of this hyperspectral signature may have interesting mechanistic and intervention implications. This will require the generation of a large library of hyperspectral images of known features of cellular or non-cellular structures in physiological and pathophysiological models. Taken together with detailed characterisation of autofluorescent signals

following pharmacological intervention, would provide a deeper understanding of which molecules or metabolites were changing their fluorescent signals. Our small, but appropriately powered study, identified a unique biological autofluorescent fingerprint associated with CCI and associated neuropathic pain in males and females demonstrating the power of this technology. In a field of research which is heavily contested, our non-reductionist approach to identifying sex differences in pain, paves the way for further larger studies to investigate if pharmacological intervention, for instance, can change this fluorescent signal.

To date, neuroscientists have looked towards defined cellular bodies such as neurons or more recently, glial cells to explain the presence of pain pathology. This narrow view and hence limited approach has had serious implications on the progress of our understanding of pain physiology and the molecular mechanism associated with it. Indeed, as recently reviewed by Piers et al.[29] many studies have investigated relatively large cell populations that are heterogeneous in their phenotype. This has made it inherently difficult to identify which subpopulations may actually participate in the exaggerated pain state. Importantly, evidence suggests that the phenotype of the cells engaged during exaggerated pain closely correlated with the pain type. Despite the heterogeneity of the cells, this common neuroimmune microcircuit underlying the pain supports our methodological process of "CCI mask" generation.

The hyperspectral autofluorescence imaging approach outlined in this study is a major advance in the repertoire of tools available to neuroscientists to identify biomarkers of pain and develop diagnostic tools to identify novel contributors to pain in patients. This study represents a new frontier in pain research; we have demonstrated for the first time that a cell type free approach can identify autofluorescent changes following nerve injury in regions that encompass cellular bodies as well as the extracellular matrix. These are the regions where cumulative changes will represent the complete picture of pain pathology. By identifying unique biological autofluorescent fingerprints associated with CCI and resultant neuropathic pain in male and female mice, our study opens up the opportunity to investigate if a similar unique autofluorescent signature can be identified in the bloods, saliva, urine or tears of mice following CCI injury. An identification of a signal associated with CCI (and the resultant neuropathic pain) in these biological samples paves the way for the development of diagnostic tools for objective measures of pain and a pathway to translation for the future of precision pain medicine in humans.

Author contributions

The idea of this study was conceived by MRH and EMG, study design was developed by MRH, SM, VS and AGA, experiments were conducted by VS, AGA and SBM, data analysis was primarily conducted by MEG, with some contributions from VS, all authors contributed to the preparation of the manuscript.

Declaration of Competing Interest

MEG is affiliated with Quantitative Pty Ltd. who currently manufactures bespoke hyperspectral equipment for microscopy purposes.

Acknowledgements

This work was funded by the Australian Research Council Centre of Excellence for Nanoscale Biophotonics CE140100003. We would like to acknowledge Drs Jacob Thomas and Jonathan Jacobsen for their contribution towards von Frey animal work conducted in this study.

Appendix A. Supplementary data

Supplementary data to this article can be found online at https://doi.org/10.1016/j.nbd.2021.105528.

References

Campbell, J., et al., 2020a. Multispectral Characterisation of Mesenchymal Stem/Stromal Cells: Age, Cell Cycle, Senescence, and Pluripotency. Vol. 11251 PWB. SPIE.
Campbell, J.M., et al., 2019. Non-destructive, label free identification of cell cycle phase in cancer cells by multispectral microscopy of autofluorescence. BMC Cancer 19, 1242. https://doi.org/10.1186/s12885-019-6463-x.
Campbell, J.M., et al., 2020b. Ageing human bone marrow mesenchymal stem cells have depleted NAD (P) H and distinct multispectral autofluorescence. GeroScience 1–10.
Cox, T.R., Erler, J.T., 2011. Remodeling and homeostasis of the extracellular matrix: implications for fibrotic diseases and cancer. Dis. Model. Mech. 4, 165–178.
Gosnell, M.E., Anwer, A.G., Cassano, J.C., Sue, C.M., Goldys, E.M., 2016a. Functional hyperspectral imaging captures subtle details of cell metabolism in olfactory neurosphere cells, disease-specific models of neurodegenerative disorders. Biochim. Biophys. Acta (BBA)-Mol. Cell Res. 1863, 56–63.
Gosnell, M.E., et al., 2016b. Quantitative non-invasive cell characterisation and discrimination based on multispectral autofluorescence features. Sci. Rep. 6.
Grace, P.M., Hutchinson, M.R., Manavis, J., Somogyi, A.A., Rolan, P.E., 2010. A novel animal model of graded neuropathic pain: utility to investigate mechanisms of population heterogeneity. J. Neurosci. Methods 193, 47–53.
Grace, P.M., et al., 2012. Harnessing pain heterogeneity and RNA transcriptome to identify blood-based pain biomarkers: a novel correlational study design and bioinformatics approach in a graded chronic constriction injury model. J. Neurochem. 122, 976–994. https://doi.org/10.1111/j.1471-4159.2012.07833.x.
Grace, P.M., Hutchinson, M.R., Maier, S.F., Watkins, L.R., 2014. Pathological pain and the neuroimmune interface. Nat. Rev. Immunol. 14, 217–231.
Grace, P.M., et al., 2016. Nitroxidative signaling mechanisms in pathological pain. Trends Neurosci. 39, 862–879. https://doi.org/10.1016/j.tins.2016.10.003.
Habibalahi, A., et al., 2019a. Optimized Autofluorescence Spectral Signature for Non-Invasive Diagnostics of Ocular Surface Squamous Neoplasia (OSSN), 7, pp. 141343–141351.
Habibalahi, A., Bala, C., Allende, A., G. Anwer, A., Goldys, Ewa M., 2019b. Novel Automated Non Invasive Detection of Ocular Surface Squamous Neoplasia Using Multispectral Autofluorescence Imaging. The Ocular Surface 17 (3), 540–550. https://doi.org/10.1016/j.jtos.2019.03.003.
Habibalahi, A., et al., 2020. Non-invasive real-time imaging of reactive oxygen species (ROS) using multispectral auto-fluorescence imaging technique: a novel tool for redox biology, 101561.
Jacobsen, J.H.W., et al., 2016. Novel imaging tools for investigating the role of immune signalling in the brain. Brain Behav. Immun. 58, 40–47. https://doi.org/10.1016/j.bbi.2016.04.014.
Ji, R.R., Chamessian, A., Zhang, Y.Q., 2016. Pain regulation by non-neuronal cells and inflammation. Science 354, 572–577. https://doi.org/10.1126/science.aaf8924.
Kawasaki, Y., et al., 2008. Distinct roles of matrix metalloproteases in the early-and late-phase development of neuropathic pain. Nat. Med. 14, 331–336.
Mahbub, S.B., 2017. Unsupervised Hyperspectral Unmixing Analysis for Label-Free Quantitative Identification of Native Fluorophores in a Biological Sample by a Robust Dependent Component Analysis (RoDECA). Macquarie University, Faculty of Science and Engineering, Department of ….
Mahbub, S.B., Plöschner, M., Gosnell, M.E., Anwer, A.G., Goldys, E.M., 2017. Statistically strong label-free quantitative identification of native fluorophores in a biological sample. Sci. Rep. 7, 1–12.
Mahbub, S.B., et al., 2019. Non-invasive monitoring of functional state of articular cartilage tissue with label-free unsupervised hyperspectral imaging. Sci. Rep. 9, 4398. https://doi.org/10.1038/s41598-019-40942-7.
Mahbub, S.B., et al., 2021. Non-invasive assessment of exfoliated kidney cells extracted from urine using multispectral autofluorescence features. Sci. Rep. 11, 1–10.
Massey Jr., F.J., 1951. The Kolmogorov-Smirnov test for goodness of fit. J. Am. Stat. Assoc. 46, 68–78.
Møller, M.F., 1993. A scaled conjugate gradient algorithm for fast supervised learning. Neural Netw. 6, 525–533.
Monteiro, C.A.S., et al., 2021. Optical imaging of cleavage stage bovine embryos using hyperspectral and confocal approaches reveals metabolic differences between on-time and fast-developing embryos. Theriogenology 159, 60–68.
Nicotra, L., Loram, L.C., Watkins, L.R., Hutchinson, M.R., 2012. Toll-like receptors in chronic pain. Exp. Neurol. 234, 316–329. https://doi.org/10.1016/j.expneurol.2011.09.038.
Nicotra, L., Tuke, J., Grace, P., Rolan, P.E., Hutchinson, M.R., 2014. Sex differences in mechanical allodynia: how can it be preclinically quantified and analyzed? Front. Behav. Neurosci. 8, 40.
Nightingale, S., 2012. The neuropathic pain market. Nat. Rev. Drug Discov. 11, 101–102. https://doi.org/10.1038/nrd3624.
Peirs, C., Dallel, R., Todd, A.J., 2020. Recent advances in our understanding of the organization of dorsal horn neuron populations and their contribution to cutaneous mechanical allodynia. J. Neural Transm. 127, 505–525. https://doi.org/10.1007/s00702-020-02159-1.
Rigaud, M., et al., 2008. Species and strain differences in rodent sciatic nerve anatomy: implications for studies of neuropathic pain. Pain 136, 188–201. https://doi.org/10.1016/j.pain.2008.01.016.
Singh, S., Bray, M.A., Jones, T.R., Carpenter, A.E., 2014. Pipeline for illumination correction of images for high-throughput microscopy. J. Microsc. 256, 231–236. https://doi.org/10.1111/jmi.12178.

Tajerian, M., Clark, J.D., 2019. Spinal matrix metalloproteinase 8 regulates pain after peripheral trauma. J. Pain Res. 12, 1133–1138. https://doi.org/10.2147/jpr.S197761.
Treuting, P.M., Dintzis, S.M., Montine, K.S., 2017. Comparative Anatomy and Histology: A Mouse, Rat, and Human Atlas. Academic Press.
Wang, Z., Gerstein, M., Snyder, M., 2009. RNA-Seq: a revolutionary tool for transcriptomics. Nat. Rev. Genet. 10, 57–63.
WHO, 2020. Opioid overdose. https://www.who.int/news-room/fact-sheets/detail/opioid-overdose.